



Ultra-wideband polarization-independent nano-metamaterial-based solar energy absorber in infrared, visible and ultraviolet regimes

Mohammad Jakir Hossain¹ · Md. Alim Uddin¹ · Akash Shaha¹ ·
Mohammad Rashed Iqbal Faruque² · K. S. Al-mugren³

Received: 23 May 2024 / Accepted: 6 August 2024

© The Author(s), under exclusive licence to Springer Science+Business Media, LLC, part of Springer Nature 2024

Abstract

This article presents a numerical analysis of a very thin concentric octagonal elliptical ring resonator (CORR) with a cylindrical rod optical nano-metamaterial absorber (ONMMA) that is designed to absorb solar energy in the infrared, visible, and ultraviolet ranges. The ONMMA is made of gold and nickel resonators on a quartz substrate with a gold plate ground material. The absorption rate of the ONMMA is over 90% from 593.84–829.28 THz, with an average absorption rate of 93.891%. This means that the ONMMA can absorb more than 80% of the energy in the infrared, visible, and a small portion of the ultraviolet range. It also has an absorption rate of over 75% from 226.64–853.04 THz, with an average absorption rate of 88.945%. This covers the entire visible spectrum, with a small portion in the infrared and ultraviolet regions. The design has an operational bandwidth of 200–920 THz, with an average absorption rate of 86.424%. The ONMMA achieves a maximum absorption rate of 99.866% at 705.44 THz. The design of the octagonal ONMMA ensures that it is not affected by the polarization of the incident light and can absorb energy even at oblique angles up to 60 degrees. The study also analyzed the effects of different materials and geometrical parameters on the absorption characteristics, as well as the distribution of surface current, magnetic field, electric field, and power loss. The proposed ONMMA has promising applications in infrared detection, solar cells, and multicolor imaging applications.

Keywords Nano-metamaterial absorber · Ultra-wideband · Infrared · Visible · Ultraviolet · Infrared detection · Solar energy absorber · Multicolor imaging

✉ Mohammad Jakir Hossain
jakir@duet.ac.bd

✉ Mohammad Rashed Iqbal Faruque
rashed@ukm.edu.my

¹ Electrical and Electronic Engineering, Dhaka University of Engineering & Technology (DUET), Gazipur, Bangladesh

² Space Science Centre (ANGKASA), Universiti Kebangsaan Malaysia UKM, 43600 Bangi, Selangor, Malaysia

³ Physics Department, Science College, Princess Nourah Bint Abdulrahman University, Riyadh, Saudi Arabia

1 Introduction

Optical metamaterials have potential in photonics and can be engineered to have desired electromagnetic properties. Optical metamaterials have led to increased research in electromagnetic absorbers due to their significant importance (Feng et al. 2020). Research on electromagnetic absorbers has increased due to their importance in solar energy harvesting (Liu et al. 2021), photovoltaic devices (Cui et al. 2016), and sensing (Beruete and Jáuregui-López 2020). There are two types of absorbers: resonant absorbers, which absorb specific frequencies, and broadband absorbers, which absorb a wide range of frequencies (Zhou et al. 2020). Different types of metamaterial geometries have been analyzed, including the double split-ring resonator, U-shaped SRR, chiral metamaterial (Tian et al. 2017) and multi-layer structure (Zheng et al. 2024a). Various types of electromagnetic absorbers have been developed for different frequency ranges, such as microwave (Liu et al. 2018), terahertz (Wang et al. 2022), infrared (Bağmancı et al. 2017), and visible frequencies (Hakim et al. 2022). Different structures and materials, including carbon nanotubes dispersed in polymers (Kang et al. 2019), graphene-based applications (Li et al. 2024a; Zheng et al. 2024b, 2024c), hash-shaped geometries, dual-band designs, and gold layers with dielectric spacers, have been investigated to achieve high absorption in specific frequency ranges. These absorbers show polarization insensitivity and wide-angle absorption capabilities (Zhang et al. 2016). Gold nanoparticles with a gold reflector and a dielectric spacer also result in high absorption in the visible spectrum, with polarization insensitivity at certain incidence angles (Yan et al. 2014). Different nanostructured materials have been utilized for industrial heater applications (Ali et al. 2024; Agravat et al. 2024a, 2024b). A metal-dielectric-metal structure has been created using a Cu/Si₃N₄/Cu stack on a silicon substrate. This structure can absorb almost all of the visible light. It has been found that this structure can achieve an average absorbance of over 80% in the visible range of 400–700 nm (Zhu and Jay Guo 2012). Another type of absorber called a terahertz metamaterial absorber, has been developed using four metallic gold rings. This absorber can absorb light regardless of its polarization. The absorption peaks of this absorber are due to the resonance state of the individual rings, and adding another metallic ring can produce even more absorption peaks (Wang et al. 2015). Researchers have also used a genetic algorithm to create an optical metamaterial with a wide range of absorption in the mid-infrared wavelength range (Bossard et al. 2014). This metamaterial is also polarization-insensitive. Plasmonic nanoantenna patches made of ZnS and gold have been placed over a thick gold layer to create an efficient and wide-band plasmonic absorber in the infrared spectrum (Xu et al. 2021). A research group has demonstrated that including multiple sublattices in a metamaterial perfect absorber can enhance absorption peaks in the mid-infrared range (Hou et al. 2021). Another absorber has been built for the visible spectrum using four split-ring resonators. This absorber can achieve high absorption for both TE and TM polarizations due to the coupling effect between gold and GaAs (Cheng et al. 2023). Finally, a silica-chromium-silica layer has been used to create an absorber structure without patterning the metamaterial. This structure can absorb light in the visible and near-infrared ranges with wavelengths of 0.4–1.4 μm (METAL, L.O.R. 2018). In a study (Jiang et al. 2018), a tunable terahertz absorber called bulk-Dirac-Semimetal (BDS) is introduced. By applying a biasing potential, the absorption properties of the BDS layer can be adjusted. A new absorber structure, consisting of split circular resonators with metallic split rings and graphene stacks in SiO₂, has been developed. This structure offers a tunable absorption coefficient exceeding 0.9 within the frequency range of 2.58–3.56

THz (Dong et al. 2017). Plasmonic graphene-based absorbers with metallic cross structures provide absorption peaks using graphene (Xiong et al. 2015). A structure with graphene/MgF₂ stacks on gold film shows two absorption peaks and a nanosecond photothermal effect (Su et al. 2015). A tunable absorber is designed using a random hill climbing algorithm to achieve a wide bandwidth of absorption (Torabi et al. 2017). Researchers have developed a broadband metasurface solar absorber that operates in both the infrared and visible ranges of the solar spectrum (Liang et al. 2023; Li et al. 2024b). Using an evolutionary algorithm, they optimized the unit cell area to enhance absorption bandwidth (Heidari and Sedighy 2018). The absorber, made of a cross-shaped metasurface with gold nanorods, achieves multiple absorption resonances across the entire solar spectrum (Khan et al. 2018). A broadband terahertz absorber has been developed using eight gold nano-resonators arranged in a symmetrical pattern. This absorber is capable of absorbing a wide range of frequencies, from near-infrared to visible light (Azad et al. 2016). The authors suggest a new architecture that utilizes a multifunctional metamaterial absorber to absorb longwave IR energy (8–12 μm) directly in a thin-film lithium niobate layer. This absorber also serves as the contacts for the two-terminal detector. The device achieves a narrowband absorption (560 nm FWHM at 10.73 μm) with high efficiency (86%) (Suen et al. 2017). The authors have proposed a new type of absorber that can perform multiple functions. This absorber is integrated with a detector that can detect both mid-wave infrared (MWIR) and long-wave infrared (LWIR) wavelengths. The detector is made using a very thin InAs/GaSb Type-II superlattice (T2SL) interband cascade detector (Montoya et al. 2017). The research shows that these multifunctional metamaterials can effectively detect specific wavelengths in the infrared spectrum. This can be useful for improving infrared imaging in various applications.

In this research, we have presented the design of a nano-metamaterial-based wideband solar absorber using gold and nickel as resonators, and it was investigated in terms of reflectance, absorbance, and various properties. The suggested construction was examined by concurrently altering materials and various geometrical factors. The design of ONMMA has an absorption rate of over 90% from 593.84–829.8 THz, with an average absorption rate of 93.891%. This covers more than 50% of the visible range and a small portion of the ultraviolet range. Additionally, the ONMMA has an absorption rate of over 75% from 226.64–853.04 THz, with an average absorption rate of 88.945%. This covers the entire visible spectrum, with a small portion in the infrared and ultraviolet regions. The operational bandwidth of the design is 200–920 THz, with an average absorption rate of 86.424%. The ONMMA achieves a maximum absorption rate of 99.866% at 705.44 THz.

2 Design and modelling

The suggested design of a metamaterial-based wideband solar exploiter is depicted in Fig. 1. Where Fig. 1a gives a three-dimensional schematic using materials, Fig. 1b displays a front view, and Fig. 1c shows the side view using parameters of the design. The structure includes an octagonal elliptical shape of nickel inside a square box shape of nickel. A circular gold ring is located above the octagonal elliptical nickel shape. Also, a square shape of gold is located on the nickel at the center as resonators and a gold ground plane is separated by a Quartz (Fused) substrate. The specifications of substrate material (Quartz) are $\tan\delta=0.0004$, $\epsilon=3.75$, thermal conductivity=5 [W/K/m], $\text{Rho}=2200$ [kg/m^3], heat capacity 0.7 [KJ/K/Kg], thermal expan. 0.5×10^{-6} /K and $\mu=1$. Quartz can withstand very

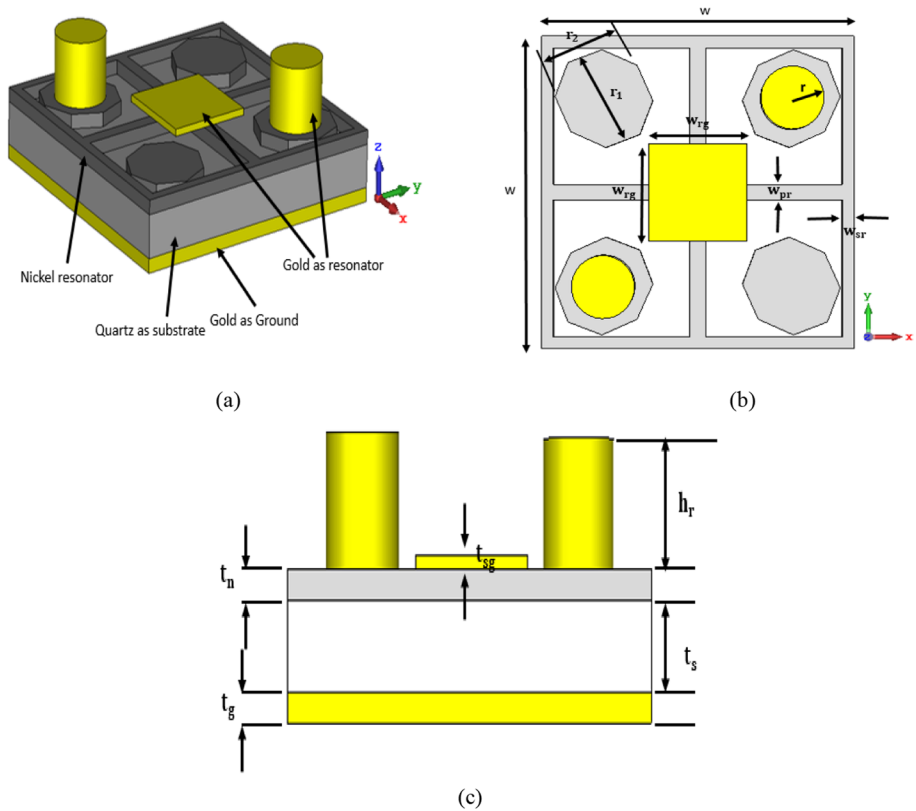


Fig.1 **a** The geometry of the proposed unit cell, **b** front view, and **c** side view

high temperatures with a melting point of about 1,710 °C (3,110°F). It has low thermal expansion, maintaining its structural integrity under thermal stress. Its low thermal expansion and high thermal conductivity also enable it to resist thermal shock, allowing it to endure rapid temperature changes without cracking or breaking. Due to its thermal stability, quartz is commonly used in applications like furnace linings, high-temperature windows, laboratory crucibles, and semiconductor manufacturing. Gold has an Electric conductivity of 4.561×10^7 [S/m], Thermal conductivity = 314 [W/K/m], $Rho = 19,320$ [kg/m³], Heat capacity of 0.13 [KJ/K/Kg], Thermal expan. 14×10^{-6} /K and $\mu = 1$. Nickel has electric conductivity 144×10^7 [S/m], thermal conductivity = 91 [W/K/m], $Rho = 8900$ [kg/m³], heat capacity 0.45 [KJ/K/Kg], thermal expan. 13.1×10^{-6} /K and $\mu = 600$. The radius of gold resonators is considered 'r', the radius of octagonal elliptical nickel resonators is 'r_{on}', the height of gold ring resonators is 'h_r', the thickness of square shape gold 't_{sg}' the thickness of nickel 't_n', the thickness of the substrate as 't_s', the thickness of the ground plane as 't_g', and the length and width of the substrate and ground plane as 'w', the length and width of square shape the gold plate 'w_{rg}', the width of plus shape nickel resonator 'w_{pr}' the width of square shape nickel resonator 'w_{sr}' that is the overall width of the geometry. The structural parameters for proposed unit cell construction are shown in Table 1.

Table 1 Structural parameters for proposed unit cell construction

Parameter	W	W _{sr}	W _{pr}	W _{fg}	t _g	t _s
Value(nm)	400	15	20	125	20	60
Parameter	t _n	t _{sg}	h _r	r ₁	r ₂	r
Value(nm)	20	10	90	65	60	40

The proposed structure is analyzed using Computer Simulation Technology (CST). Positioned in the x - y plane, it is subjected to a transverse electric field directed from $+z$ to $-z$. The boundary conditions are configured with unit cells in the x - y plane, $E_t=0$ at Z_{min} , and Z_{max} is set to open (add space). A mesh, which divides the structure into small elements, is generated to create a discretized model. CST provides an adaptive mesh automatically for accurate results, although the mesh settings can be manually adjusted for more precise control.

The relation between absorption (A), reflectance (R), and transmittance (T) is given as,

$$A = 1 - R - T$$

Where the reflection coefficient (S_{11}) and transmission coefficient (S_{21}),

$$R = |S_{11}| \text{ and } T = |S_{21}|$$

The gold material used in the design has a skin depth for light ranging from 5.55 nm to 2.59 nm, which is smaller than the thickness of the material. Consequently, the transmittance is zero (Abohmra et al. 2020).

$$A = 1 - R \quad (1)$$

Electron Beam Lithography (EBL) as a possible manufacturing method. EBL uses a focused electron beam to create specific patterns on a substrate coated with resist.

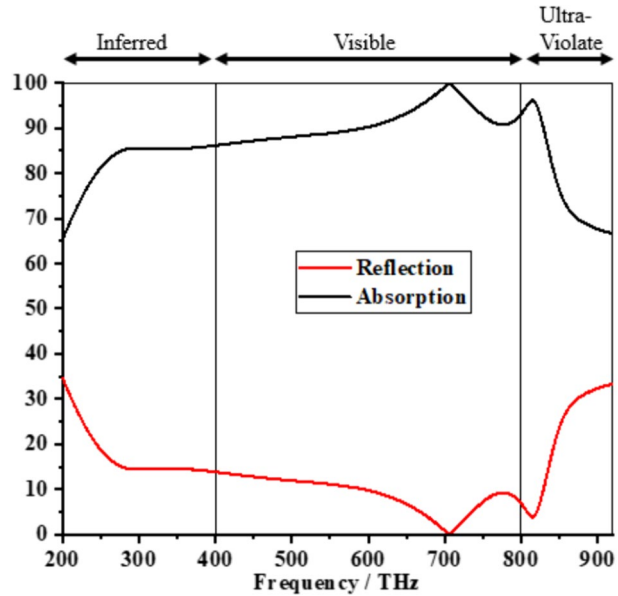
3 Results and discussion

This section discusses the simulated results and behaviors of ONMMA. It starts by discussing the absorption characteristics in Sect. 3.1. Then, it describes how the polarization insensitivity angles (0° , 90° , and 180°) and incident angles (0° , 15° , 30° , 45° , and 60°) affect ONMMA in Sect. 3.2. Section 3.3 illustrates the different geometric parametric analyses and material characteristics of absorption. Additionally, Sect. 3.4 discusses the E-field, H-field, and surface current distributions, as well as the power loss distribution, which is responsible for the absorption mechanism.

3.1 Absorption characteristics of the proposed ONMMA

The absorption characteristics of the proposed ONMMA were analyzed using equation (1). The absorption exceeded 75% in the frequency range of 226.64–853.04 THz, covering a small portion of infrared light wave frequencies, full visible frequency ranges, and a small section of ultraviolet frequencies. In the range of 593.84–829.28 THz, absorption was over 90%, spanning more than 50% of visible frequencies and a small ultraviolet range. Overall, the proposed ONMMA achieved 86.424% absorption in the sunlight range of 200–920

Fig. 2 The absorption and reflection rates of the proposed structure



THz, making it an ultra-wideband absorber. Figure 2 shows the absorption and reflection of the proposed ONMMA. The two peak absorptions are 99.866% and 96.19% at frequencies 705.44 THz and 814.88 THz.

3.2 Polarization insensitivity and incident angle stability

The study examined how the absorber's effectiveness is affected by different angles at which electromagnetic (EM) waves hit it. The angles at which the waves hit and refract have a significant impact on the amount of reflection that occurs. Figure 3a, b illustrates the polarization angle (ϕ) and the oblique incident angle (θ) of the EM wave hitting the absorber. The EM wave travels towards the negative z-axis. The red circle represents the area where the incident angle θ can range from 0 to 180 degrees, and the green circle represents the area where the angle ϕ can range from 0 to 360 degrees, encompassing the electric and magnetic field vectors of the EM wave.

The absorption characteristics of the design were analyzed at different polarization angles (ϕ), showing that the ONPMA performed well even at angles up to 180°. The research on ONPMA architecture for solar cell implementation focuses on complying with the design framework for capturing different polarizations of EM radiation from the sun. Designing an effective solar cell is challenging as it requires containing arbitrary polarizations of EM radiation. Numerical analysis showed that the proposed ONPMA had maximum absorption of 99.866%, 99.849%, and 99.952% with a total average absorption of 86.424%, 86.413%, and 86.415% in the range 200–920 THz for polarisation angles of 0°, 90°, and 180° respectively, making it a promising candidate for solar energy collection. Figure 3c and d show that as the angle of incidence increases, there is a decrease in average absorption and a shift towards higher frequencies. Higher incidence angles reduce the coupling impact and the wave-confining ability of the dielectric layer. Specular reflection was used to determine absorption, which revealed that most reflected energy was concentrated in a certain

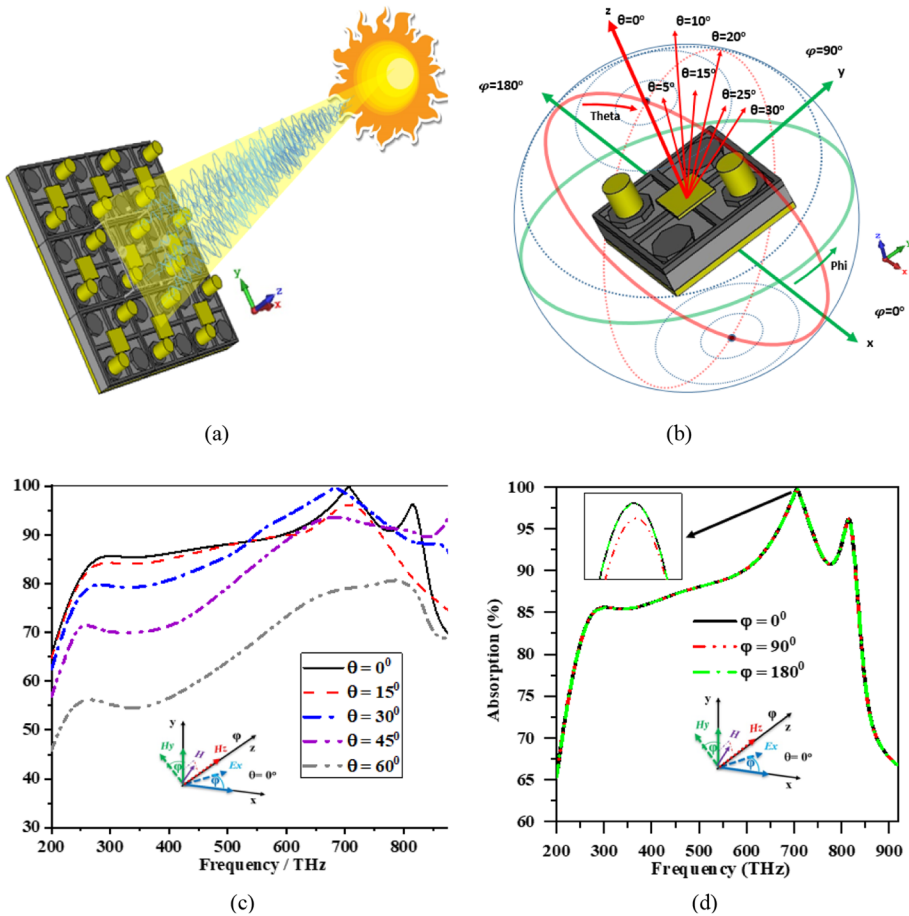


Fig. 3 **a** Incident of EM wave on ONPMA **b** Indication of Phi and Theta angle of incident EM wave on ONPMA, **c** Incident angle, **d** Polarization insensitivity

direction. Based on the numerical analysis, the highest peaks are 99.866%, 96.199%, 99.502%, 98.350%, and 80.680%, at a frequency of 705.44THz, 706.88 THz, 683.84 THz, 891.20 THz and 782.48 THz; Also, a total average absorption in the range 200–920 THz is 86.424%, 85.199%, 86.547%, 81.950% and 66.930% for incident angles of 0°, 15°, 30°, 45°, and 60° respectively. The numerical analysis identified the highest absorption peaks at various incident angles.

3.3 Parametric analysis

This section examines the results of the parametric analysis. It investigates how the performance of the metamaterial is affected by the type of substrates used, the influence of different conducting materials on scattering parameters, variations in

structural dimensions, and the impact of different thicknesses of shapes. The following subsection concentrates on studying the distribution of surface current, electric field, magnetic field, and power distributions.

3.3.1 Dependence on geometric parameters

This section analyzes the results of the parametric analysis. It investigates how the performance of the absorber is affected by the variations in geometric parameters of the ground, substrate, and conducting materials. The influence of variations in structural dimensions, shapes, and the impact of different material thicknesses changes the absorption characteristics, which are shown in Fig. 4. The absorption data with variations in geometric parameters is shown in Table 2.

Table 2 shows the maximum peak absorption to be 99.866%, the maximum average absorption to be 86.424%, and the maximum bandwidth to be 626.40 THz with absorption above 75%. Additionally, at a dimension of $200 \times 200 \text{ um}^2$, the absorption is above 90% at 235.44 THz. The best performance is achieved with a substrate thickness of 60 nm. The absorption characteristics also depend on the conducting elliptical radius, with the best performance observed at $r_1/r_2 = 125 \text{ nm}/125 \text{ nm}$. Similarly, the maximum

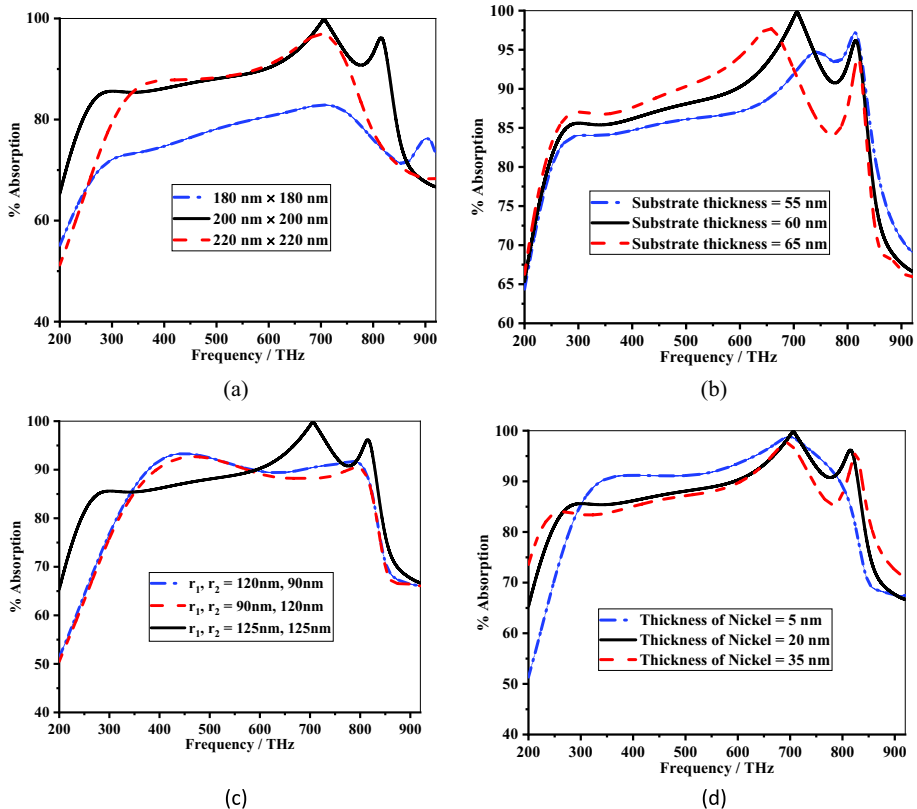


Fig. 4 Different absorption characteristics of **a** changes in dimensions of substrate and ground; **b** various substrate thicknesses; **c** different elliptical shapes; and **d** several thicknesses of nickel conductor

Table 2 Comparison table for dependence on geometric parameters

Different parameters	Values (nm)	75% Bandwidth		90% Bandwidth		Overall avg. absorp	Max absorp	Peak freq
		Freq. range (THz)	Avg. absorp	Freq. range (THz)	Avg. absorp			
Thickness of nickel	5	261.92–835.76	91.375	338.96–794.72	93.214	86.310	98.814	698.24
	20	226.64–853.04	88.945	593.84–829.28	93.891	86.424	99.866	705.44
	35	204.32–879.68	87.225	606.08–743.60; 808.40–837.2	93.788	86.331	97.590	693.20
Elliptical shape radius (r_1, r_2)	$r_1 = 125, r_2 = 125$	226.64–853.04	88.945	593.84–829.28	93.891	86.424	99.866	705.44
	$r_1 = 90, r_2 = 120$	296.48–840.08	88.620	394.40–573.68	91.537	82.795	92.686	467.84
	$r_1 = 120, r_2 = 90$	292.88–840.8	89.531	377.84–583.76; 684.56–808.40	91.625	83.765	93.312	448.40
Substrate thickness	55	230.96–871.76	87.084	675.20–832.88	93.682	85.299	97.181	813.44
	60	226.64–853.04	88.945	593.84–829.28	93.891	86.424	99.866	705.44
	65	221.60–845.84	89.109	488.00–714.80; 806.96–827.84	93.432	86.412	97.761	654.32
Dimension of substrate and ground	180 × 180	408.80–809.12; 889.04–913.52	79.378	–	–	75.769	82.882	705.44
	200 × 200	226.64–853.04	88.945	593.84–829.28	93.891	86.424	99.866	705.44
	220 × 220	282.08–813.44	88.467	579.44–752.96	93.753	82.803	96.885	700.40

average and peak absorption alter with changing conductive nickel thickness, and the best performance is obtained at a thickness of 20 nm.

3.3.2 Dependence on materials

This study examines how the absorber’s performance is impacted by changes in the materials used for the ground, substrate, and conducting patch. The absorption characteristics are influenced by the different properties of these materials, as depicted in Fig. 5. Table 3 presents the absorption data for various material variations.

Different metamaterials have been found to alter absorption characteristics, as shown in Table 3. When using different conducting materials, the highest average absorption, maximum peak, and width of absorption above 75% and 90% are changes with using materials. The best absorption characteristics were observed with gold rings and octagonal nickel as the conductive materials. On the other hand, when using various substrate materials, the highest peak, average absorption, and width are achieved with quartz as the substrate. As for the ground material, copper and silver yield the highest peak absorption but show overall absorptions are less. However, overall, the best performance is obtained

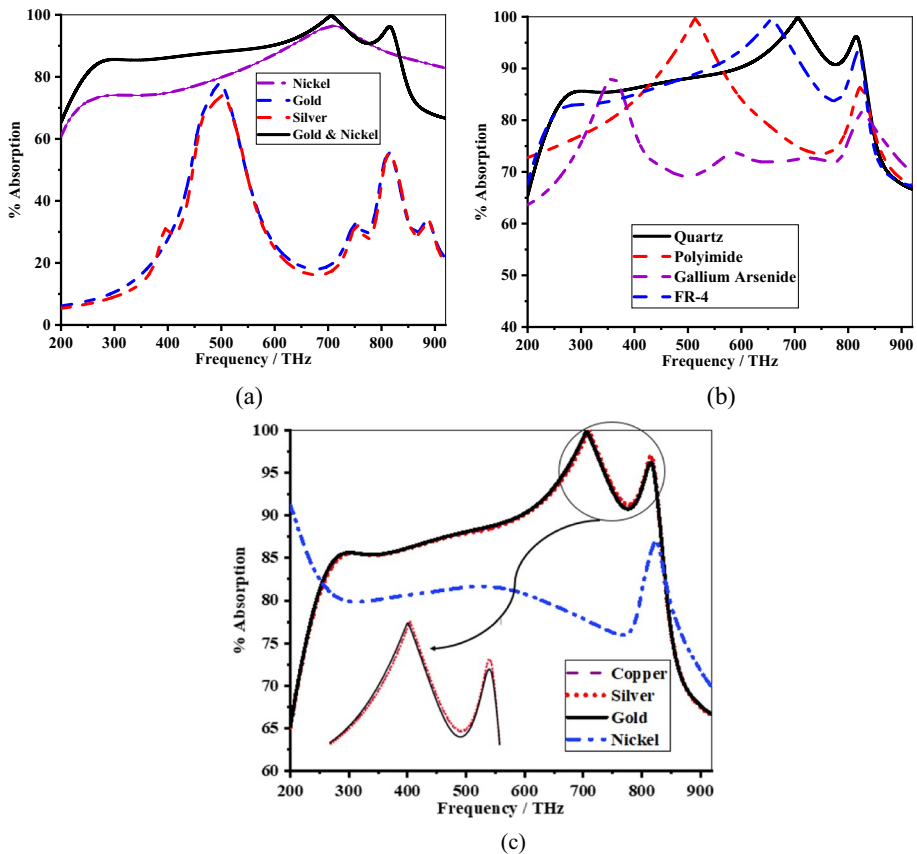


Fig. 5 Different absorption characteristics of **a** changes in conducting patch materials; **b** various substrate materials; **c** different ground materials

Table 3 Comparison table for variation of material on absorption characteristics

Different parameters	Values (nm)	75% Bandwidth		90% Bandwidth		Overall Avg. absorp	Max absorp	Peak freq
		Freq. range (THz)	Avg. absorp	Freq. range (THz)	Avg. absorp			
Conducting material	Gold with Nickel	226.64–853.04	88.945	593.84–829.28	93.891	86.424	99.866	705.44
	Gold	483.68–508.16	76.698	–	–	31.015	77.681	496.64
	Silver	–	–	–	–	29.582	73.929	500.96
Substrate material	Nickel	404.48–920	86.27	630.56–783.20	93.66	82.34	96.41	709.04
	Quartz	226.64–853.04	88.945	593.84–829.28	93.891	86.424	99.866	705.44
	Beryllia	256.16–702.56; 781.04–856.64	83.864	454.16–526.88	94.799	80.809	99.829	513.92
	GaAs	297.20–410.96; 796.88–873.92	80.708	–	–	73.725	88.108	359.12
Ground material	Gold	226.64–853.04	88.945	593.84–829.28	93.891	86.424	99.866	705.44
	Silver	227.36–853.04	88.886	598.16–828.56	94.057	86.346	99.971	709.04
	Copper	226.64–853.04	88.890	596.00–829.28	94.010	86.368	99.976	708.32
Nickel	200–873.92	80.59	200–205.76	90.58	80.05	91.14	200	

when using quartz as the substrate, nickel, and gold as the conducting patch, and gold as the ground material. With these materials, the proposed design achieves a peak absorption of 99.866%, absorption above 75% in the total range of 626.40 THz, absorption above 90% in the total range of 235.44 THz, and a total average absorption of 86.424% in the ranges 200–920 THz.

3.4 Mechanisms of absorption

This section analyzed the properties of absorption of the proposed ONMMA. In the numerical analysis, the finite integration technique (FIT) method-based CST Electromagnetic (EM) simulator is used to numerically study a specific structure. The boundary conditions are set up with a unit cell boundary condition in the x and y directions, and an open boundary condition in the z -direction. The electromagnetic wave propagates along the z -axis, with the electric field parallel to the x -axis and the magnetic field parallel to the y -axis.

3.4.1 Analysis of surface current, electric field, and magnetic field distribution

An analysis was conducted to understand how absorption works by examining the surface current and electric field at two specific resonance frequencies: 705.44 THz and 814.88 THz. These frequencies were chosen because they represent the points where absorption is at its highest level. When absorption is perfect, the absorbers' electric and magnetic responses match those of the incoming wave, resulting in resonance frequencies. Figure 6 illustrates that the absorber causes a significant concentration of circulating current along the edge of the nickel resonators. Further investigation reveals the presence of parallel and anti-parallel surface currents traveling across the nickel slabs, which generate an electric resonance in the absorber. Additionally, the flowing current creates a magnetic resonance.

Another method of comprehending the absorption process involves analyzing the distribution of the electric field and magnetic field at resonant frequencies shown in Fig. 7 and Fig. 8 respectively. Figure 7 demonstrates that the electric field is primarily

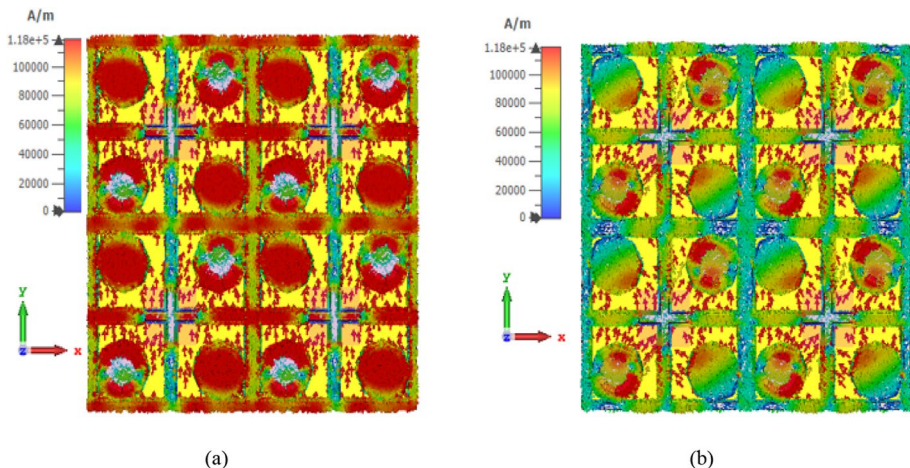


Fig. 6 Surface current distribution at **a** 705.44 THz, **b** 814.88 THz

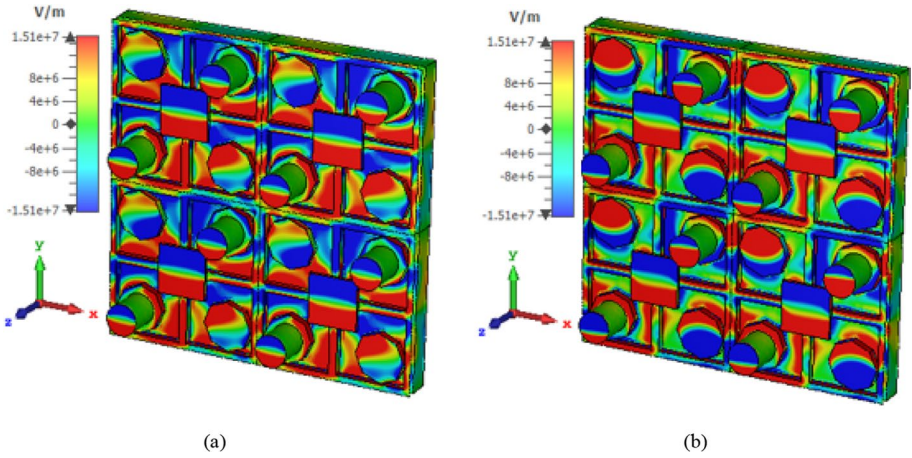


Fig. 7 E-field distribution at **a** 705.44 THz, **b** 814.88 THz

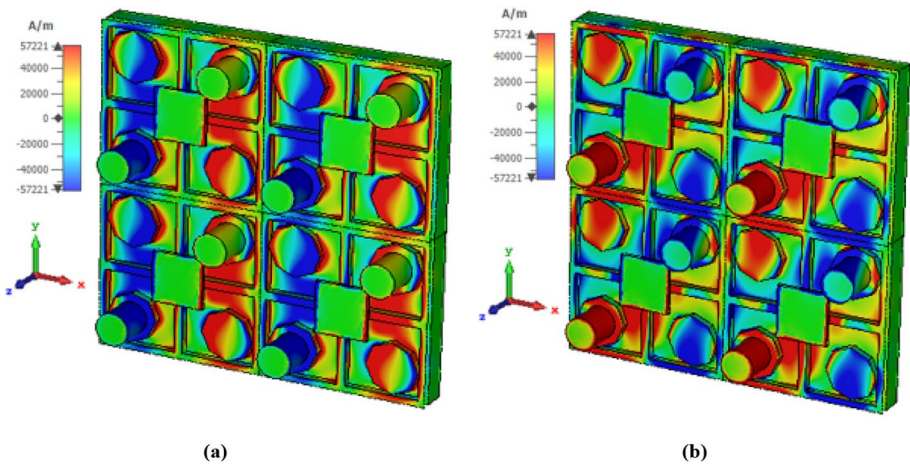


Fig. 8 H-field distribution at **a** 705.44 THz, **b** 814.88 THz

concentrated along the edges of the nickel slabs. This behavior resembles that of electric dipoles, which are accountable for electrical resonance. Additionally, the strong electric field, resembling a dipole, generates surface charges that oscillate in conjunction with the electric field, resulting in magnetic resonance.

3.4.2 Analysis of power loss distribution

The study also analyzed power loss distributions at two resonant frequencies, 705.44 THz and 814.88 THz, to gain a better understanding of how absorption happens in the dielectric and metallic layers. Figure 9 demonstrates that the resonators have a significant impact on wideband absorption, even though quartz has a low loss tangent of 0.0004. This is because

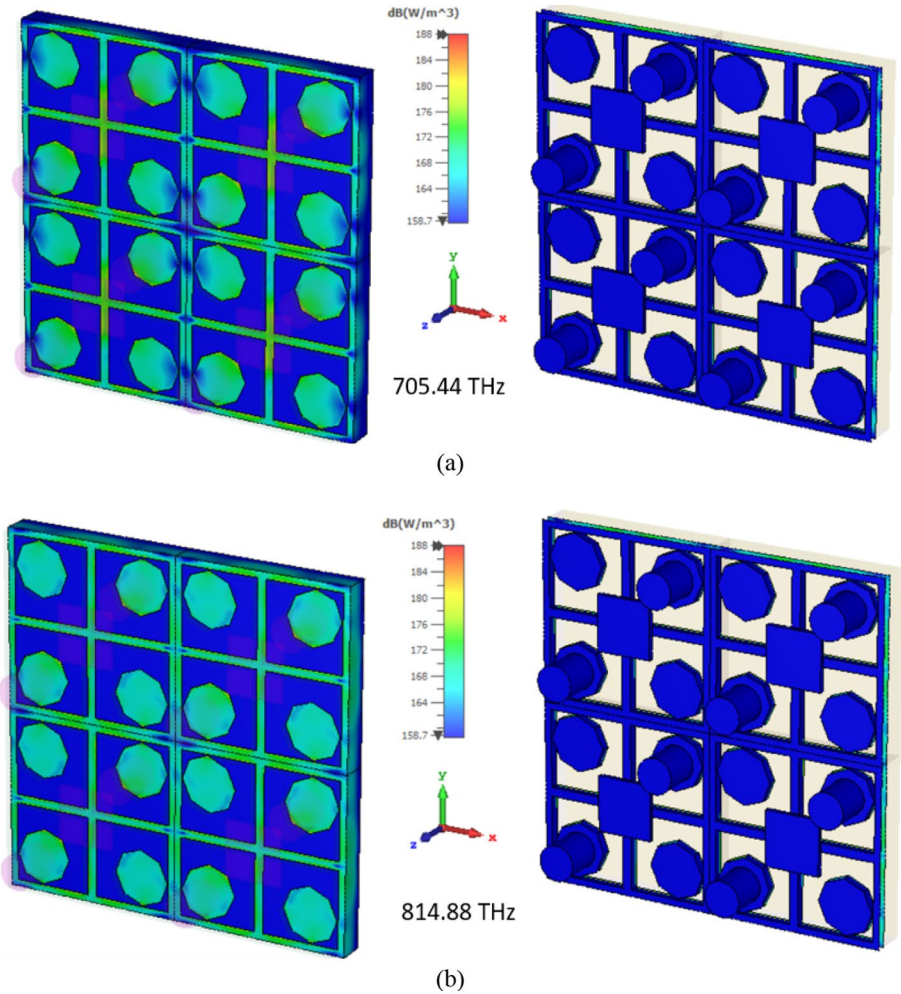


Fig. 9 Power loss distribution at **a** 705.44 THz and **b** 814.88 THz

the metallic layer tends to have higher losses than the dielectric in the infrared frequency range, making it more responsible for wideband absorption.

The suggested absorber is being compared to absorbers from previous studies that have similar properties, such as ultra-wideband absorption and functioning in the infrared, visible, and ultraviolet frequency ranges. The data in Table 4 shows that the suggested absorber has a significantly average absorption, peak absorption and compact dimension across a wider frequency range. With these qualities, the suggested absorber has the potential to be used in infrared detection, solar energy harvesting, and multicolor imaging applications.

Table 4 Comparison of proposed ONMMA with relevant works

Refs	Operation bandwidth	Dimensions (nm ³)	Materials	Average absorption	Peak Absorption	Published Year
41	341–810	600 × 600 × 180	Au, SiO ₂	83%	92%	2015
42	384–674	380 × 380 × 150	W, SiO ₂	60%	99%	2019
43	155–428	1000 × 1000 × 310	Au, SiO ₂	80.24%	96.40	2019
44	150–1500	200 × 200 × 75	Ni, SiO ₂	80%	98%	2021
45	21.75–150	4000 × 4000 × 2300	Ti, Ge, Si ₃ N ₄	78%	98.6%	2021
46	176–600	200 × 190 × 545	SiO ₂ , Ti, MgF ₂ , Au, TiO	82%	99.5%	2022
Proposed	200–920	200 × 200 × 190	Qz, Au, Ni	86.424	99.866	–

4 Conclusion

This article suggests using a small concentric cylindrical gold ring on an elliptical nickel conductor, along with a square sheet of gold placed in the center of a plus-shaped nickel structure, to create an ultra-wideband absorber. This device is used for harvesting solar energy and multicolor imaging in the infrared, visible, and ultraviolet frequency ranges of the solar spectrum, which is between 200 and 920 THz. The size of the device is $200 \times 200 \times 190 \text{ nm}^3$ and it consists of four layers (Au-Qz-Ni-Au). The designed device has a high absorption rate, with absorption above 90% in a range of 235.44 THz bandwidth and above 75% in a range of 626.40 THz bandwidth. The maximum absorption rate is 99.866% at a frequency of 705.44 THz, and the average absorption rate in the entire range of 200–920 THz is 86.424%. The article also analyzes the properties of the device, such as the magnetic field, electric field, surface current distribution, and power loss distribution, to understand how it absorbs solar energy. Finally, a comparison with other similar devices is presented, which demonstrates that the proposed device has better characteristics in terms of size, absorption rate, and peak absorption. Therefore, the proposed device has great potential for applications in solar energy harvesting, infrared detector, and multicolor imaging applications.

Acknowledgements This research acknowledged by the Fundamental Research Grant Scheme (FRGS), MOE, Malaysia, Code: FRGS/1/2022/TK07/UKM/02/22. Moreover, this research acknowledges to the Princess Nourah bint Abdulrahman University Researchers Supporting Project number (PNURSP2024R10), Princess Nourah bint Abdulrahman University, Riyadh, Saudi Arabia.

Author contributions Mohammad Jakir Hossain, Md. Alim Uddin and Akash Shaha made substantial contributions to design, analysis and characterization and preparing the manuscript. Mohammad Rashed Iqbal Faruque and K. S. Al-mugren participated in the idea, implementation and critical revision of the article for key intellectual content and provided essential instructions for analytical purposes.

Funding The authors have not disclosed any funding.

Data Availability All the data is available within the manuscript.

Declarations

Conflict of interest The authors have not disclosed any competing interests.

References

- Abohmra, A., Abbas, H., Al-Hasan, M., Mabrouk, I.B., Alomainy, A., Imran, M.A., Abbasi, Q.H.: Terahertz antenna array based on a hybrid perovskite structure. *IEEE Open J. Antennas Propag.* **1**, 464–471 (2020)
- Agravat, D., Patel, S.K., Als Salman, O.: Investigation of graphene-perovskite integration for enhanced absorption of solar thermal absorber for industrial heating applications. *Int. J. Therm. Sci.* **201**, 109029 (2024a)
- Agravat, D., Patel, S.K., Als Salman, O.: Nanostructured metal-oxide materials for solar energy absorption and conversion for industrial heater applications. *Int. J. Therm. Sci.* **200**, 108951 (2024b)
- Ali, N.B., Agravat, D., Patel, S.K., Armghan, A., Aliqab, K., Alsharari, M.: Investigation of graphene based disk-square integration resonator for enhanced solar absorption using machine learning for solar heaters. *Alex. Eng. J.* **102**, 192–199 (2024)
- Azad, A.K., Kort-Kamp, W.J.M., Sykora, M., Weisse-Bernstein, N.R., Luk, T.S., Taylor, A.J., Dalvit, D.A.R., Chen, H.T.: Metasurface broadband solar absorber. *Sci. Rep.* **6**, 6–11 (2016). <https://doi.org/10.1038/srep20347>

- Bağmancı, M., Karaaslan, M., Ünal, E., Akgöl, O., Karadağ, F., Sabah, C.: Broad-band polarization-independent metamaterial absorber for solar energy harvesting applications. *Physica E* **90**, 1–6 (2017)
- Beruete, M., Jáuregui-López, I.: Terahertz sensing based on metasurfaces. *Adv. Opt. Mater.* **8**(3), 1900721 (2020)
- Bossard, J.A., Lin, L., Yun, S., Liu, L., Werner, D.H., Mayer, T.S.: Near-ideal optical metamaterial absorbers with super-octave bandwidth. *ACS Nano* **8**, 1517–1524 (2014). <https://doi.org/10.1021/nn4057148>
- Cheng, Y., Qian, Y., Luo, H., Chen, F., Cheng, Z.: Terahertz narrowband perfect metasurface absorber based on micro-ring-shaped GaAs array for enhanced refractive index sensing. *Physica E Low-Dimens. Syst. Nanostruct.* **146**, 115527 (2023)
- Cui, L., Huang, M.Y., You, Y.M., Zhang, Y.J., Li, G.M., Liu, S.L., Liu, C.K.: Electric and magnetic resonances in optical metamaterial for efficient absorption enhancement in ultrathin CdTe-based photovoltaic cells. *Opt. Mater. Express* **6**(5), 1480–1487 (2016)
- Dong, Y., Liu, P., Di, Yu., Li, G., Yang, L.: A Tunable Ultra broadband ultrathin terahertz absorber using graphene stacks, *IEEE antennas wirel. Propag. Lett.* **16**, 1115–1118 (2017). <https://doi.org/10.1109/LAWP.2016.2623316>
- Feng, L., Huo, P., Liang, Y., Xu, T.: Photonic metamaterial absorbers: morphology engineering and interdisciplinary applications. *Adv. Mater.* **32**(27), 1903787 (2020)
- Hakim, M.L., Alam, T., Islam, M.S., Salaheldeen, M., M., Almalki, S.H., Baharuddin, M.H., Alsaif, H. and Islam, M.T.: Wide-oblique-incident-angle stable polarization-insensitive ultra-wideband metamaterial perfect absorber for visible optical wavelength applications. *Materials* **15**(6), 2201 (2022)
- Heidari, M.H., Sedighy, S.H.: Broadband wide-angle polarization-insensitive metasurface solar absorber. *J. Opt. Soc. Am. A* **35**, 522 (2018). <https://doi.org/10.1364/JOSAA.35.000522>
- Hou, E., Qin, Z., Liang, Z., Meng, D., Shi, X., Yang, F., Liu, W., Liu, H., Xu, H., Smith, D.R., Liu, Y.: Dual-band metamaterial absorber with a low-coherence composite cross structure in mid-wave and long-wave infrared bands. *Opt. Express* **29**(22), 36145–36154 (2021)
- Jiang, Y., Xinguo, W., Wang, J., Wang, J.: Tunable terahertz absorber based on bulkdirac-semimetal metasurface. *IEEE Photonics J.* **10**, 1–7 (2018). <https://doi.org/10.1109/JPHOT.2018.2866281>
- Kang, S., Qian, Z., Rajaram, V., Caliskan, S.D., Alù, A., Rinaldi, M.: Ultra-narrowband metamaterial absorbers for high spectral resolution infrared spectroscopy. *Adv. Opt. Mater.* **7**(2), 1801236 (2019)
- Katrodiya, D., Jani, C., Sorathiya, V., Patel, S.K.: Metasurface based broadband solar absorber. *Opt. Mater.* **89**, 34–41 (2019)
- Khan, A.D., Khan, A.D., Khan, S.D., Noman, M.: Light absorption enhancement in trilayered composite metasurface absorber for solar cell applications. *Opt. Mater. (amst)* **84**, 195–198 (2018). <https://doi.org/10.1016/j.optmat.2018.07.009>
- Li, W., Liu, M., Cheng, S., Zhang, H., Yang, W., Yi, Z., Sun, T.: Polarization independent tunable bandwidth absorber based on single-layer graphene. *Diam. Relat. Mater.* **142**, 110793 (2024)
- Li, W., Liu, Y., Ling, L., Sheng, Z., Cheng, S., Yi, Z., Ahmad, S.: The tunable absorber films of grating structure of AlCuFe quasicrystal with high Q and refractive index sensitivity. *Surf. Interfaces* **48**, 104248 (2024)
- Liang, S., Xu, F., Li, W., Yang, W., Cheng, S., Yang, H., Jiang, P.: Tunable smart mid infrared thermal control emitter based on phase change material VO₂ thin film. *Appl. Therm. Eng.* **232**, 121074 (2023)
- Liu, Z., Liu, X., Huang, S., Pan, P., Chen, J., Liu, G., Gu, G.: Automatically acquired broadband plasmonic-metamaterial black absorber during the metallic film-formation. *ACS Appl. Mater. Interfaces.* **7**(8), 4962–4968 (2015)
- Liu, C., Qi, L., Wu, M.: Triple-broadband infrared metamaterial absorber with polarization-independent and wide-angle absorption. *Opt. Mater. Express* **8**(8), 2439–2448 (2018)
- Liu, H., Xie, M., Ai, Q., Yu, Z.: Ultra-broadband selective absorber for near-perfect harvesting of solar energy. *J. Quant. Spectrosc. Radiat. Transfer* **266**, 107575 (2021)
- METAL, L.O.R., 2018. Huixu Deng, Zhigang Li, Liliana Stan, Daniel Rosenmann, David Czaplewski, Jie Gao, and Xiaodong Yang. Design for optical metamaterial design for optical metamaterial absorber, 20
- Montoya, J.A., Tian, Z.B., Krishna, S., Padilla, W.J.: Ultra-thin infrared metamaterial detector for multicolor imaging applications. *Opt. Express* **25**(19), 23343–23355 (2017)
- Naveed, M.A., Bilal, R.M.H., Baqir, M.A., Bashir, M.M., Ali, M.M., Rahim, A.A.: Ultrawideband fractal metamaterial absorber made of nickel operating in the UV to IR spectrum. *Opt. Express* **29**(26), 42911–42923 (2021)
- Su, Z., Yin, J., Zhao, X.: Terahertz dual-band metamaterial absorber based on graphene/MgF₂ multilayer structures. *Opt. Express* **23**, 1679 (2015). <https://doi.org/10.1364/OE.23.001679>

- Suen, J.Y., Fan, K., Montoya, J., Bingham, C., Stenger, V., Sriram, S., Padilla, W.J.: Multifunctional metamaterial pyroelectric infrared detectors. *Optica* **4**(2), 276–279 (2017)
- Tian, X., Yin, L., Li, D.: Current situation and trend of fabrication technologies for three-dimensional metamaterials. *Opto-Electron. Eng.* **44**(1), 69–76 (2017)
- Torabi, E.S., Fallahi, A., Yahaghi, A.: Evolutionary optimization of graphene-metal metasurfaces for tunable broadband terahertz absorption. *IEEE Trans. Antennas Propag.* **65**, 1464–1467 (2017). <https://doi.org/10.1109/TAP.2016.2647580>
- Wang, B.X., Zhai, X., Wang, G.Z., Huang, W.Q., Wang, L.L.: Design of a four-band and polarization-insensitive terahertz metamaterial absorber. *IEEE Photonics J.* **7**, 1–8 (2015). <https://doi.org/10.1109/JPHOT.2014.2381633>
- Wang, B.X., Wu, Y., Xu, W., Yang, Z., Lu, L., Pi, F.: Quad-band terahertz metamaterial absorber enabled by an asymmetric I-type resonator formed from three metallic strips for sensing application. *Sens. Diagn.* **1**(1), 169–176 (2022)
- Xiong, F., Zhang, J., Zhu, Z., Yuan, X., Qin, S.: Ultra-broadband, more than one order absorption enhancement in graphene with plasmonic light trapping. *Sci. Rep.* **5**, 1–8 (2015). <https://doi.org/10.1038/srep16998>
- Xu, H., Hu, L., Lu, Y., Xu, J., Chen, Y.: Dual-band metamaterial absorbers in the visible and near-infrared regions. *J. Phys. Chem. C* **123**(15), 10028–10033 (2019)
- Xu, F., Lin, L., Fang, J., Huang, M., Wang, F., Su, J., Li, S., Pan, M.: Broadband solar absorber based on square ring cross arrays of ZnS. *Micromachines* **12**(8), 909 (2021)
- Yan, M., Dai, J., Qiu, M.: Lithography-free broadband visible light absorber based on a mono-layer of gold nanoparticles. *J. Opt.* **16**(2), 025002 (2014). <https://doi.org/10.1088/2040-8978/16/2/025002>
- Zhang, X., Fan, Y., Qi, L., Li, H.: Broadband plasmonic metamaterial absorber with fish-scale structure at visible frequencies. *Opt. Mater. Express* **6**(7), 2448–2457 (2016)
- Zhang, B., Li, Z., Hu, Z., Zhang, J., Wang, J.: Analysis of a bidirectional metamaterial perfect absorber with band-switchability for multifunctional optical applications. *Results Phys.* **34**, 105313 (2022)
- Zheng, Y., Zhao, W., Song, Q., Ma, C., Yi, Z., Zeng, Q., Yan, J.: Analysis of solar absorption and thermal radiation properties of a multi-layer structure. *Int. J. Therm. Sci.* **203**, 109172 (2024)
- Zheng, Y., Wang, Z., Yi, Z., Cheng, S., Ma, C., Tang, B., Ahmad, S.: A wide-band solar absorber based on tungsten nano-strip resonator group and graphene for near-ultraviolet to near-infrared region. *Diam. Relat. Mater.* **142**, 110843 (2024)
- Zheng, R., Liu, Y., Ling, L., Sheng, Z., Yi, Z., Song, Q., Sun, T.: Ultra wideband tunable terahertz metamaterial absorber based on single-layer graphene strip. *Diam. Relat. Mater.* **141**, 110713 (2024)
- Zhou, J., Liu, Z., Liu, X., Fu, G., Liu, G., Chen, J., Wang, C., Zhang, H., Hong, M.: Metamaterial and nanomaterial electromagnetic wave absorbers: structures, properties and applications. *J. Mater. Chem. C* **8**(37), 12768–12794 (2020)
- Zhou, Y., Qin, Z., Liang, Z., Meng, D., Xu, H., Smith, D.R., Liu, Y.: Ultra-broadband metamaterial absorbers from long to very long infrared regime. *Light Sci. Appl.* **10**, 138 (2021). <https://doi.org/10.1038/s41377-021-00577-8>
- Zhu, P., Jay Guo, L.: High performance broadband absorber in the visible band by engineered dispersion and geometry of a metal-dielectric-metal stack. *Appl. Phys. Lett.* (2012). <https://doi.org/10.1063/1.4771994>

Publisher's Note Springer Nature remains neutral with regard to jurisdictional claims in published maps and institutional affiliations.

Springer Nature or its licensor (e.g. a society or other partner) holds exclusive rights to this article under a publishing agreement with the author(s) or other rightsholder(s); author self-archiving of the accepted manuscript version of this article is solely governed by the terms of such publishing agreement and applicable law.